Quantitative Disentanglement of the Spin Seebeck, Proximity-Induced, and Ferromagnetic-Induced Anomalous Nernst Effect in Normal-Metal–Ferromagnet Bilayers

Panagiota Bougiatioti,[1] Christoph Klewe,[1,2] Daniel Meier,[1] Orestis Manos,[1] Olga Kuschel,[3] Joachim Wollschläger,[3] Laurence Bouchenoire,[4,5] Simon D. Brown,[4,5] Jan-Michael Schmalhorst,[1] Günter Reiss,[1] and Timo Kuschel[1,6]

[1]*Center for Spinelectronic Materials and Devices, Department of Physics, Bielefeld University, Universitätsstraße 25, 33615 Bielefeld, Germany*

[2]*Advanced Light Source, Lawrence Berkeley National Laboratory, Berkeley, California 94720, USA*

[3]*Department of Physics and Center of Physics and Chemistry of New Materials, Osnabrück University, Barbarastrasse 7, 49076 Osnabrück, Germany*

[4]*XMaS, European Synchrotron Radiation Facility, Grenoble 38043, France*

[5]*Department of Physics, University of Liverpool, Liverpool L69 7ZE, United Kingdom*

[6]*Physics of Nanodevices, Zernike Institue for Advanced Materials, University of Groningen, Nijenborgh 4, 9747 AG Groningen, Netherlands*

(Received 17 February 2017; revised manuscript received 9 August 2017; published 29 November 2017)

We identify and investigate thermal spin transport phenomena in sputter-deposited $Pt/NiFe_2O_x$ ($4 \geq x \geq 0$) bilayers. We separate the voltage generated by the spin Seebeck effect from the anomalous Nernst effect (ANE) contributions and even disentangle the ANE in the ferromagnet (FM) from the ANE produced by the Pt that is spin polarized due to its proximity to the FM. Further, we probe the dependence of these effects on the electrical conductivity and the band gap energy of the FM film varying from nearly insulating $NiFe_2O_4$ to metallic $Ni_{33}Fe_{67}$. A proximity-induced ANE could only be identified in the metallic $Pt/Ni_{33}Fe_{67}$ bilayer in contrast to $Pt/NiFe_2O_x$ ($x > 0$) samples. This is verified by the investigation of static magnetic proximity effects via x-ray resonant magnetic reflectivity.

DOI: 10.1103/PhysRevLett.119.227205

In the emerging fields of spintronics [1] and spin caloritronics [2], phenomena such as the spin Hall effect [3] and the spin Seebeck effect (SSE) [4,5] enable the generation, manipulation, and detection of spin currents in ferro(i)magnetic insulators (FMIs). The most common path to detect a spin current is to use a normal metal (NM) with a large spin Hall angle, such as Pt [6], Ta [7], Pd [8], and W [9] on top of a ferromagnetic (FM) material. The inverse spin Hall effect (ISHE) [10] then leads to the conversion of the spin current into a transverse charge voltage in the NM.

Pt is employed frequently for generating and detecting pure spin currents, if adjacent to a FMI, though the possibility of magnetic proximity effects (MPEs) has to be taken into account. Because of its close vicinity to the Stoner criterion [11] the FM can potentially generate a Pt spin polarization at the interface. Consequently, this might induce additional parasitic effects preventing the correct interpretation of the measured ISHE voltage. Therefore, a comprehensive investigation regarding the magnetic properties of the NM/FM interface is required to distinguish the contributions of such parasitic voltages from the ISHE voltage generated by a pure spin current.

In the case of the SSE, the driving force for the spin current in the FM or FMI is a temperature gradient. When a spin current is generated parallel to a temperature gradient, it is generally attributed to the longitudinal spin Seebeck effect (LSSE) [4,5]. However, when using the ISHE in an adjacent NM for the spin current detection, a proximity-induced ANE [12] can not only contaminate the LSSE signal, but also an additional ANE contribution could be present in case of studying ferromagnetic metals (FMMs) or semiconducting ferro(i)magnets [13,14]. Primarily NM/FMI bilayers have been investigated, while LSSE studies on NM/FMM are quite rare. On this topic, Holanda *et al.* [15] reported the observation of the LSSE signal separated from the ANE contribution in permalloy (Py) by using Pt/NiO/Py trilayer samples.

Additionally, Ramos *et al.* [14,16–18] and Wu *et al.* [19] individually investigated the LSSE in magnetite, which is conducting at room temperature (RT) and, thus, has an ANE contribution induced from the FM. They identified the LSSE in Pt/Fe_3O_4 [14] and $CoFeB/Fe_3O_4$ bilayers [19] by using temperatures below the conductor-insulator transition of magnetite (Verwey transition at 120 K) in order to exclude any FM-induced ANE contribution. Ramos *et al.* further investigated the ANE in bulk magnetite without any Pt [16] and concluded that the ANE contributions for Pt/Fe_3O_4 bilayers and multilayers should be quite small [17,18]. In addition, Lee *et al.* [20] and Uchida *et al.* [21,22] discussed that in Pt/FMM multilayers both the LSSE and ANE contribute, but did not disentangle the effects quantitatively. Hence, a clear quantitative disentanglement of the LSSE in the FMM, the ANE in the FMM, and the proximity-induced ANE in the NM is still pending.

Some groups used Cu or Au interlayers to suppress the MPE in NM/FMM bilayers [23–25]. However, a promising

technique to distinguish between the LSSE and proximity-induced ANE was first proposed by Kikkawa *et al.* [23,26]. In their study, the voltage measured transverse to the thermal gradient in in-plane magnetized (IPM) and out-of-plane magnetized (OPM) configurations, leads to the sufficient separation of the aforestated contributions. So far, this technique was only used to study the proximity-induced ANE in NM/FMI bilayers. It has not yet been applied to fully conducting NM/FMM bilayers for the separation of the LSSE and ANE contributions in the FMM. In our Letter, we extend this technique to identify all three contributions quantitatively: the LSSE, the ANE in the FM, and the proximity-induced ANE. We will use this separation for investigating these effects in Pt on different FM materials such as nearly insulating $NiFe_2O_4$, semiconductinglike $NiFe_2O_x$ ($4 > x > 0$), and metallic $Ni_{33}Fe_{67}$. At this point it is worth noting that Bauer *et al.* [2] introduced the term "spin Seebeck effect" for FMI systems based on magnon transport while for the spin-dependent thermal creation of moving electrons in metals and semiconductors they suggested the term "spin-dependent Seebeck effect" (SDSE). In our Letter we will not distinguish between SSE and SDSE in the conducting materials; thus, we just use the term SSE throughout the Letter.

To confirm or exclude any possible static MPE at the interface of a Pt/FM hybrid structure, element-selective x-ray resonant magnetic reflectivity (XRMR) has been used due to its sensitivity to magnetic moments at interfaces [27,28]. XRMR measurements were performed at the XMaS beamline BM28 at European Synchrotron Radiation Facility (Grenoble, France) [29], at RT. Details of the XRMR technique, experiment, and data processing can be found in the Supplemental Material [30] (Chap. II, including Ref. [31]).

We fabricated the films on $MgAl_2O_4$ (MAO) substrates by sputter deposition [32] starting from pure high-resistive $NiFe_2O_4$ (NFO) (~160 nm) up to the metallic $Ni_{33}Fe_{67}$ (10.4 nm) with intermediate $NiFe_2O_{x_1}$ (60 nm) and $NiFe_2O_{x_2}$ (35 nm), with $4 > x_1 > x_2 > 0$, see Supplemental Material [30] (Chap. I). Twin FM layers have been prepared with and without Pt *in situ* deposited on top, in a range of (2.7–3.5) nm, by *in situ* covering one FM layer with a mask to maintain the same deposition conditions for the FM in both samples. Magnetic and structural characterizations of the samples are included in the Supplemental Material [30] (Chap. I, including Ref. [33]).

Figures 1(a)–1(c) illustrate the measurement geometries that we have employed for the separation of the three effects. In the IPM geometries [Figs. 1(a) and 1(c)] the application of an out-of-plane temperature gradient ∇T in the presence of an in-plane magnetic field along the x axis induces a transverse voltage along the y axis. While measuring in this IPM configuration with Pt on top [IPM-Pt, Fig. 1(a)], we detect the LSSE voltage together with both ANE contributions, i.e., FM induced and proximity induced. However, in the IPM geometry without

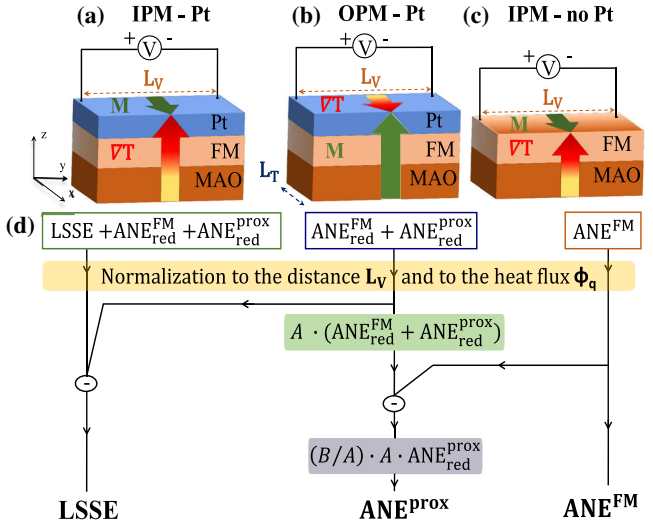

FIG. 1. Schematic illustration of (a),(c) in-plane magnetized and (b) out-of-plane magnetized geometries, introducing the temperature gradient ∇T, the magnetization vector $\boldsymbol{M}$, the distance between the contacts L_V, and the total length of the sample L_T, respectively. (d) Flow chart for the quantitative separation of both ANE contributions from the LSSE voltage. The light green and grey areas correspond to the intermediate steps determining the correction factors A and B, respectively, taking into account the reduction of the ANE signal due to the additional Pt layer (spin polarized and/or nonmagnetic).

Pt [IPM-no Pt, Fig. 1(c)], we are only sensitive to the ANE contribution from the FM.

The ISHE voltage is determined according to the relation

$$\boldsymbol{E}_{\mathrm{ISHE}} \propto \boldsymbol{J}_s \times \boldsymbol{s} \tag{1}$$

where $\boldsymbol{E}_{\mathrm{ISHE}}$, $\boldsymbol{J}_s$, and $\boldsymbol{s}$ denote the electric field induced by the ISHE, the spin current which enters the spin detector material, and the spin-polarization vector, respectively. The spin current $\boldsymbol{J}_s$ depends on the applied temperature gradient via the SSE coefficient S_{SSE}. Moreover, the ANE contribution is described by the relation

$$\boldsymbol{E}_{\mathrm{ANE}} \propto \nabla T \times \boldsymbol{M} \tag{2}$$

where $\boldsymbol{E}_{\mathrm{ANE}}$ and $\boldsymbol{M}$ denote the electric field induced by ANE, and the magnetization vector of the FM, respectively.

In the OPM geometry with Pt on top [OPM-Pt, Fig. 1(b)], the application of an in-plane temperature gradient ∇T together with an out-of-plane magnetic field generates a transverse voltage attributed to the FM-induced and proximity-induced ANE. In this configuration, the LSSE cannot be detected, since no out-of-plane spin current with the proper spin-polarization direction is generated [23]. One major issue is to consider the reduction of the ANE signal upon a placement of a Pt layer [14]. All ANE contributions measured with Pt on top have in general reduced contributions, which is indicated by the subscript "red" in Fig. 1 and throughout the Letter. Additional contributions to the

measured voltage in this configuration are discussed in the Supplemental Material [30] (Chap. IV, including Refs. [34–39]).

Figure 1(d) explains the flow chart for the quantitative disentanglement of the three effects. As a first step, the electric field is calculated from the measured voltages by normalizing to the distance of the electric contacts L_V. Then, this electric field is divided by the heat flux ϕ_q that runs through the sample. The normalization to the heat flux, as suggested by Sola *et al.* [40,41], allows for eliminating the systematic errors due to the thermal interface resistances and thermal contacts resulting in the effective comparison between IPM and OPM configurations as well as in the comparability of our results. Further details on the temperature gradient application and the heat flux normalization can be found in the Supplemental Material [30] (Chaps. III and IV, including Refs. [42,43]). To estimate the ANE reduction due to the additional Pt layer we used the ratio of conductances G of the $NiFe_2O_x$ and the Pt in a parallel arrangement [14],

$$r = \frac{G_{NiFe_2O_x}}{G_{Pt}} = \frac{\rho_{Pt}}{\rho_{NiFe_2O_x}} \frac{t_{NiFe_2O_x}}{t_{Pt}}, \quad (3)$$

with ρ the RT resistivity and t the thickness of the corresponding layer. The reduced ANE signal from the FM (ANE^{FM}_{red}) in the OPM-Pt configuration is then corrected by the factor $A = (r+1)/r$ [14] resulting in the pure $ANE^{FM} = A \times ANE^{FM}_{red}$. This correction step in our calculations is highlighted by the light green area in Fig. 1(d). Combined with the information on the ANE^{FM} from the IPM-no Pt configuration [cf. Fig. 1(c)], i.e., by subtracting the ANE^{FM} from the corrected term, this method yields a qualitative criterion for the existence or absence of proximity-induced ANE in the sample.

For a quantitative evaluation, an additional correction has to be applied to the reduced proximity-induced ANE signal (ANE^{prox}_{red}) due to the additional nonmagnetic Pt layer, while the correction A on the term has to be reversed [see light grey area in Fig. 1(d)]. The correction factor for the ANE^{prox}_{red} is given by $B = (d_I + d_{II})/d_I$ [14], where d_I and d_{II} are the thicknesses of the spin-polarized Pt layer and the nonmagnetic fraction, respectively, estimated by XRMR. Then, the corrected proximity-induced ANE contribution is denoted as $ANE^{prox} = (B/A) \times A \times ANE^{prox}_{red}$. For the polarized and unpolarized fraction of the Pt layers, the same resistivity ρ_{Pt} was used.

As an example, for the $Pt/Ni_{33}Fe_{67}$ ($Pt/NiFe_2O_{x_2}$) sample the reduction of the ANE^{FM} is estimated to be 47% (95%) by using the measured values for the RT resistivity of Pt equal to $\rho_{Pt} = 1.6 \times 10^{-7}\ \Omega\,m$ ($1.8 \times 10^{-7}\ \Omega\,m$) for a Pt film with thickness $t_{Pt} = 3.5$ nm (3.1 nm) and of the FM equal to $\rho_{Ni_{33}Fe_{67}(NiFe_2O_{x_2})} = 4.2 \times 10^{-7}\ \Omega\,m$ ($4.5 \times 10^{-5}\ \Omega\,m$) for a FM thickness of $t_{Ni_{33}Fe_{67}(NiFe_2O_{x_2})} = 10.4$ nm (35 nm). Moreover, for the metallic $Pt/Ni_{33}Fe_{67}$ bilayer the reduction of the ANE^{prox} is estimated to be 71% by considering $d_I = 1.0$ nm of spin polarized Pt layer and $d_{II} = 2.5$ nm of nonmagnetic Pt. A table with the obtained values for all samples can be found in the Supplemental Material [30] (Chap. V, including Ref. [44]). Consequently, the comparison between the voltage signals in the IPM and OPM geometries enables a quantitative separation of the ANE contributions from the LSSE signal.

Figure 2 illustrates the experimental results for the $Pt/NiFe_2O_{x_2}$ and $Pt/Ni_{33}Fe_{67}$ bilayers. By comparing the difference between the ANE^{FM} from the IPM-no Pt configuration (orange line) and the $ANE^{FM} + ANE^{prox}$ signals (corrected $ANE^{FM}_{red} + ANE^{prox}_{red}$ by A and B, as explained above, purple line) we are able to quantitatively determine the contribution from the proximity-induced ANE. For the nonmetallic $NiFe_2O_{x_2}$ bilayer [Figs. 2(a) and 2(b)] no difference can be determined between the saturation values of the ANE^{FM} data from IPM-no Pt configuration [orange line in Fig. 2(a)] and the saturation values of the $ANE^{FM} + ANE^{prox}$ signal [corrected OPM-Pt data, purple line in Fig. 2(b)], which are extracted to be $V^{sat}_{norm} = (0.18 \pm 0.02)10^{-4}$ mV W^{-1} m in both cases. Thus, the ANE^{prox} is zero and can be neglected for this sample. We conclude that the LSSE appears to be the prominent contribution to the total signal [cf. Fig. 2(a), green line]. In contrast, for the $Pt/Ni_{33}Fe_{67}$ bilayer [Figs. 2(c) and 2(d)] the $ANE^{FM} + ANE^{prox}$ is $(46 \pm 3)\%$ larger than the ANE^{FM} signal that shows the existence of the MPE. Furthermore, for the Pt/NFO bilayer both ANE^{FM} and $ANE^{FM} + ANE^{prox}$

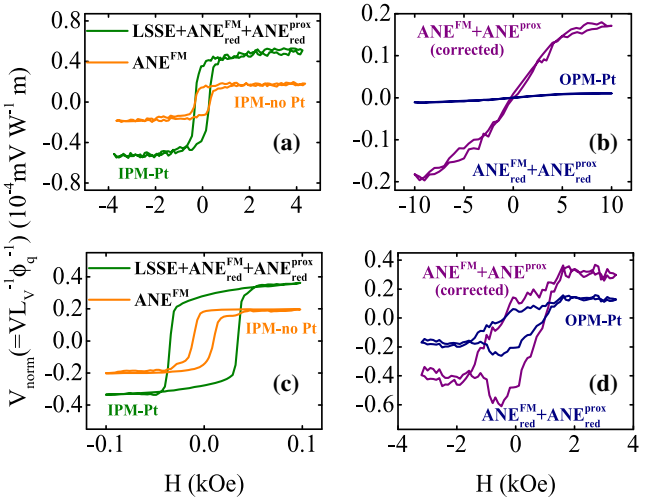

FIG. 2. Normalized voltage plotted against the magnetic field strength for (a),(b) $Pt/NiFe_2O_{x_2}$ and (c),(d) $Pt/Ni_{33}Fe_{67}$ bilayers measured in (a),(c) IPM and (b),(d) OPM geometries with the corresponding separation of the ANE contribution (FM induced and proximity induced) from the LSSE voltage. $ANE^{FM} + ANE^{prox}$ (purple) represents the calculated ANE signal after the implementation of the correction factors A and B, which correct the reduction of the measured ANE from the OPM-Pt configuration due to the additional Pt layer (spin polarized and/or nonmagnetic).

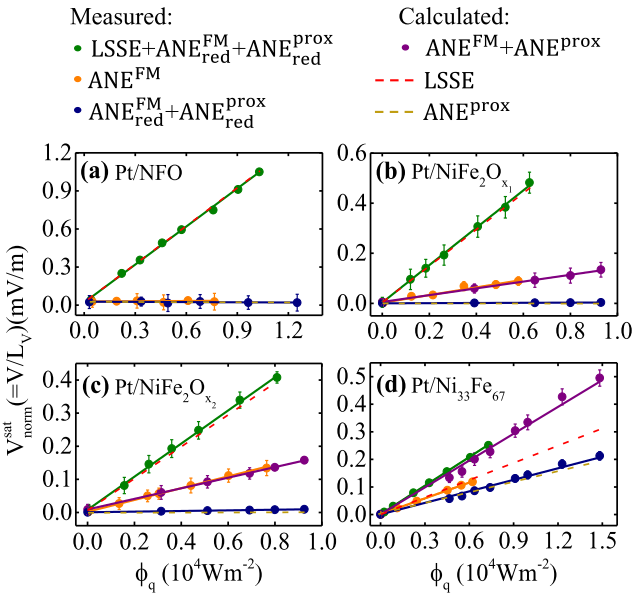

FIG. 3. Normalized voltage in saturation against the heat flux for (a) Pt/NFO, (b),(c) Pt/NiFe$_2$O$_{x_1/x_2}$, and (d) Pt/Ni$_{33}$Fe$_{67}$ samples with the corresponding separation of the ANE contribution (FM induced and proximity induced) from the LSSE voltage.

signals are zero, confirming the absence of any ANE contribution in the pure Pt/NFO bilayer [28,45].

Figure 3 illustrates the linear dependence of the voltage in saturation on ϕ_q, normalized to L_V for all samples. The dashed lines are the calculated contributions of the pure LSSE and ANE^{prox} extracted as described in the diagram of Fig. 1(d) after correcting the reduced ANE signal arising from both the FM and the spin-polarized Pt layer. In Fig. 3(a), the zero line contribution of both types of ANE indicates the absence of MPE in Pt/NFO bilayers [28,45]. The low amount of mobile charge carriers in the nearly insulating NFO leads to a vanishing ANE^{FM} contribution [13].

As shown in Figs. 3(a)–3(c), the LSSE contribution is dominant for all Pt/NiFe$_2$O$_x$ ($x > 0$) bilayers that consist of oxides. Furthermore, the absence of any proximity-induced ANE is verified, since no difference between the ANE^{FM} and the ANE^{FM} + ANE^{prox} can be identified. Additionally, for the Pt/NiFe$_2$O$_{x_2}$ bilayer the ANE^{FM} contribution is 14% larger than for the Pt/NiFe$_2$O$_{x_1}$ bilayer, pointing towards its more conducting character. For the Pt/Ni$_{33}$Fe$_{67}$ bilayer [Fig. 3(d)], the enhancement of ANE^{FM} + ANE^{prox} due to the metallic character of Ni$_{33}$Fe$_{67}$ and the MPE contribution is clearly displayed. Moreover, the ANE^{FM} and the LSSE signals are of comparable magnitude for this sample [cf. Fig. 3(d)].

Figure 4(a) shows the SSE ($S_{SSE} = V^{sat}_{norm}/\phi_q$) and ANE^{FM} ($D_{ANE^{FM}} = V^{sat}_{norm}/\phi_q$) coefficients extracted from the corresponding slopes of the curves in Fig. 3, plotted against the RT value for the measured electrical conductivity. This definition of SSE coefficient can also be referred to the spin Seebeck resistivity as recently described by

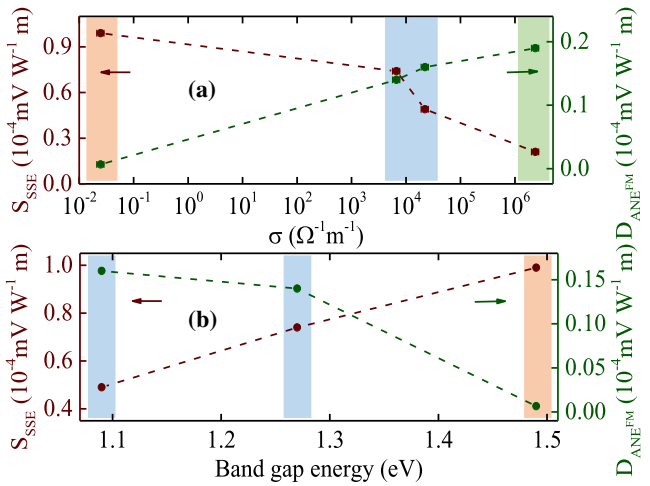

FIG. 4. SSE and ANE^{FM} coefficients as a function of (a) the electrical conductivity σ for NiFe$_2$O$_{x_1/x_2}$ (blue area), NFO (orange area), and Ni$_{33}$Fe$_{67}$ (green area) samples and (b) the optical band gap for NiFe$_2$O$_{x_1/x_2}$ and NFO samples.

Prakash *et al.* [46]. There is a pronounced increase of the $D_{ANE^{FM}}$ when the conductivity increases, whereas the S_{SSE} decreases. A probable additional thickness dependence of the extracted coefficients is discussed in the Supplemental Material [30] (Chap. VII).

Figure 4(b) depicts the dependence of the SSE and ANE^{FM} coefficients on the optical band gap for the NFO and NiFe$_2$O$_{x_1/x_2}$ bilayers. A short description of the band gap determination can be found in the Supplemental Material [30] (Chap. VIII, including Refs. [47,48]). It is clearly observed that the more conducting samples are characterized by lower band gap energies, reflecting the existence of additional electronic states in the band gap. Additionally, the ANE^{FM} coefficient increases for decreasing band gap energy, verifying the previous assumption of more mobile charge carriers at a reduced oxygen concentration. In contrast, the SSE coefficient increases for larger band gap energies.

The absence of MPE in Pt/NFO, Pt/NiFe$_2$O$_{x_1/x_2}$ samples and the presence of MPE in the metallic Pt/Ni$_{33}$Fe$_{67}$ bilayer is also confirmed by XRMR. For the Pt/Ni$_{33}$Fe$_{67}$ bilayer, we obtain a maximum Pt magnetic moment of $(0.48 \pm 0.08)\mu_B$ per spin-polarized Pt atom, consistent with earlier results [49]. The effective spin-polarized Pt thickness is calculated to be (1.0 ± 0.1) nm, similar to our previous investigations [49]. In addition, for the Pt/NFO bilayer no magnetic proximity effect was detected; however, an upper limit for the maximum magnetic moment in Pt of $0.04\mu_B$ per spin-polarized Pt atom could be estimated. Moreover, for the Pt/NiFe$_2$O$_{x_1}$ and Pt/NiFe$_2$O$_{x_2}$ samples any magnetic proximity effect could be excluded as well, with a detection limit of $0.1\mu_B$ and $0.01\mu_B$ per spin-polarized Pt atom, respectively. The method, the processing of the data, and the results are described in the Supplemental Material [30] (Chap. II). Finally, possible

MPEs can be neglected down to these limits for all samples except for the metallic $Pt/Ni_{33}Fe_{67}$ bilayer, where a distinct spin polarization in the Pt layer can be observed.

In conclusion, we investigated thermal spin transport phenomena in Pt/FM bilayers and separated the ANE in the FM- and proximity-induced ANE contributions quantitatively from the LSSE for sputter-deposited $NiFe_2O_x$ bilayers. This new compact procedure is based on the preparation of twin samples (with and without Pt), different measurement geometries, the normalization to the heat flux instead of the thermal gradient, and the determination of important correction factors to obtain quantitative LSSE and ANE values. In our Letter, we extracted the dependence of the LSSE and ANE^{FM} coefficients on the band gap energy and on the electrical conductivity of the samples. Furthermore, possible static MPEs in Pt were studied via XRMR. We found no magnetic response down to our detection limits of $0.04\mu_B$, $0.1\mu_B$, and $0.01\mu_B$ per spin-polarized Pt atom for Pt/NFO, $Pt/NiFe_2O_{x_1}$, and $Pt/NiFe_2O_{x_2}$, respectively. For the $Pt/Ni_{33}Fe_{67}$ we calculated a maximum magnetic moment of $0.48\mu_B$ per spin-polarized Pt atom. All XRMR results are well in line with the absence or presence of proximity-induced ANE contributions. As a next step, this technique of thermal transport effect separation allows us to study the individual transport effects depending on other properties of the samples, e.g., thicknesses and roughnesses. The proximity-induced thermal magnetotransport could even be extracted experimentally, and the LSSE could be identified in metallic films.

The authors gratefully acknowledge financial support by the Deutsche Forschungsgemeinschaft (DFG) within the Priority Program Spin Caloric Transport SPP 1538 (KU 3271/1-1, RE 1052/24-2) and the European Synchrotron Radiation Facility (ESRF). They additionally thank F. Freimuth, P. Gambardella, A. Hoffmann, J. Mendil, E. Saitoh, and B. Zink for valuable discussions. Christoph Klewe further acknowledges financial support from the Alexander von Humboldt Foundation.

[1] A. Hoffmann and S. D. Bader, Phys. Rev. Applied **4**, 047001 (2015).
[2] G. E. W. Bauer, E. Saitoh, and B. J. van Wees, Nat. Mater. **11**, 391 (2012).
[3] J. E. Hirsch, Phys. Rev. Lett. **83**, 1834 (1999).
[4] K. Uchida, H. Adachi, T. Ota, H. Nakayama, S. Maekawa, and E. Saitoh, Appl. Phys. Lett. **97**, 172505 (2010).
[5] K. Uchida, M. Ishida, T. Kikkawa, A. Kirihara, T. Murakami, and E. Saitoh, J. Phys. Condens. Matter **26**, 343202 (2014).
[6] L. Liu, T. Moriyama, D. C. Ralph, and R. A. Buhrman, Phys. Rev. Lett. **106**, 036601 (2011).
[7] L. Liu, C.-F. Pai, Y. Li, H. Tseng, D. Ralph, and R. Buhrman, Science **336**, 555 (2012).
[8] Z. Tang, Y. Kitamura, E. Shikoh, Y. Ando, T. Shinjo, and M. Shiraishi, Appl. Phys. Express **6**, 083001 (2013).
[9] C.-F. Pai, L. Liu, Y. Li, H. W. Tseng, D. C. Ralph, and R. A. Buhrman, Appl. Phys. Lett. **101**, 122404 (2012).
[10] E. Saitoh, M. Ueda, H. Miyajima, and G. Tatara, Appl. Phys. Lett. **88**, 182509 (2006).
[11] E. C. Stoner, Proc. R. Soc. A **165**, 372 (1938).
[12] S. Y. Huang, X. Fan, D. Qu, Y. P. Chen, W. G. Wang, J. Wu, T. Y. Chen, J. Q. Xiao, and C. L. Chien, Phys. Rev. Lett. **109**, 107204 (2012).
[13] D. Meier, T. Kuschel, L. Shen, A. Gupta, T. Kikkawa, K. Uchida, E. Saitoh, J.-M. Schmalhorst, and G. Reiss, Phys. Rev. B **87**, 054421 (2013).
[14] R. Ramos, T. Kikkawa, K. Uchida, H. Adachi, I. Lucas, M. H. Aguirre, P. Algarabel, L. Morellón, S. Maekawa, E. Saitoh, and M. R. Ibarra, Appl. Phys. Lett. **102**, 072413 (2013).
[15] J. Holanda, O. Alves Santos, R. O. Cunha, J. B. S. Mendes, R. L. Rodríguez-Suárez, A. Azevedo, and S. M. Rezende, Phys. Rev. B **95**, 214421 (2017).
[16] R. Ramos, M. H. Aguirre, A. Anadón, J. Blasco, I. Lucas, K. Uchida, P. A. Algarabel, L. Morellón, E. Saitoh, and M. R. Ibarra, Phys. Rev. B **90**, 054422 (2014).
[17] R. Ramos, T. Kikkawa, M. H. Aguirre, I. Lucas, A. Anadón, T. Oyake, K. Uchida, H. Adachi, J. Shiomi, P. A. Algarabel, L. Morellón, S. Maekawa, E. Saitoh, and M. R. Ibarra, Phys. Rev. B **92**, 220407 (2015).
[18] R. Ramos, A. Anadón, I. Lucas, K. Uchida, P. A. Algarabel, L. Morellón, M. H. Aguirre, E. Saitoh, and M. R. Ibarra, APL Mater. **4**, 104802 (2016).
[19] S. M. Wu, J. Hoffman, J. E. Pearson, and A. Bhattacharya, Appl. Phys. Lett. **105**, 092409 (2014).
[20] K.-D. Lee, D.-J. Kim, H. Y. Lee, S.-H. Kim, J.-H. Lee, K.-M. Lee, J.-R. Jeong, K.-S. Lee, H.-S. Song, J.-W. Sohn, S.-C. Shin, and B.-G. Park, Sci. Rep. **5**, 10249 (2015).
[21] K. I. Uchida, T. Kikkawa, T. Seki, T. Oyake, J. Shiomi, Z. Qiu, K. Takanashi, and E. Saitoh, Phys. Rev. B **92**, 094414 (2015).
[22] K. Uchida, H. Adachi, T. Kikkawa, A. Kirihara, M. Ishida, S. Yorozu, S. Maekawa, and E. Saitoh, Proc. IEEE **104**, 1946 (2016).
[23] T. Kikkawa, K. Uchida, Y. Shiomi, Z. Qiu, D. Hou, D. Tian, H. Nakayama, X.-F. Jin, and E. Saitoh, Phys. Rev. Lett. **110**, 067207 (2013).
[24] Y. Xu, B. Yang, C. Tang, Z. Jiang, M. Schneider, R. Whig, and J. Shi, Appl. Phys. Lett. **105**, 242404 (2014).
[25] B. F. Miao, S. Y. Huang, D. Qu, and C. L. Chien, AIP Adv. **6**, 015018 (2016).
[26] T. Kikkawa, K. Uchida, S. Daimon, Y. Shiomi, H. Adachi, Z. Qiu, D. Hou, X.-F. Jin, S. Maekawa, and E. Saitoh, Phys. Rev. B **88**, 214403 (2013).
[27] S. Macke and E. Goering, J. Phys. Condens. Matter **26**, 363201 (2014).
[28] T. Kuschel, C. Klewe, J.-M. Schmalhorst, F. Bertram, O. Kuschel, T. Schemme, J. Wollschläger, S. Francoual, J. Strempfer, A. Gupta, M. Meinert, G. Götz, D. Meier, and G. Reiss, Phys. Rev. Lett. **115**, 097401 (2015).
[29] S. D. Brown, L. Bouchenoire, D. Bowyer, J. Kervin, D. Laundy, M. J. Longfield, D. Mannix, D. F. Paul, A. Stunault,

P. Thompson, M. J. Cooper, C. A. Lucas, and W. G. Stirling, J. Synchrotron Radiat. **8**, 1172 (2001).

[30] See Supplemental Material at http://link.aps.org/supplemental/10.1103/PhysRevLett.119.227205 for additional information about the characterization of the samples, the XRMR technique and results, as well as, the heat flux calculation procedure and the thickness dependency of SSE and ANE^{FM} coefficients.

[31] L. Bouchenoire, S. D. Brown, P. Thompson, J. A. Duffy, J. W. Taylor, and M. J. Cooper, J. Synchrotron Radiat. **10**, 172 (2003).

[32] C. Klewe, M. Meinert, A. Boehnke, K. Kuepper, E. Arenholz, A. Gupta, J.-M. Schmalhorst, T. Kuschel, and G. Reiss, J. Appl. Phys. **115**, 123903 (2014).

[33] P. Bougiatioti, O. Manos, C. Klewe, D. Meier, N. Teichert, J.-M. Schmalhorst, T. Kuschel, and G. Reiss, arXiv:1708.01937.

[34] D. Meier, D. Reinhardt, M. Schmid, C. H. Back, J.-M. Schmalhorst, T. Kuschel, and G. Reiss, Phys. Rev. B **88**, 184425 (2013).

[35] M. Schmid, S. Srichandan, D. Meier, T. Kuschel, J.-M. Schmalhorst, M. Vogel, G. Reiss, C. Strunk, and C. H. Back, Phys. Rev. Lett. **111**, 187201 (2013).

[36] D. Meier, D. Reinhardt, M. van Straaten, C. Klewe, M. Althammer, M. Schreier, S. T. B. Goennenwein, A. Gupta, M. Schmid, C. H. Back, J.-M. Schmalhorst, T. Kuschel, and G. Reiss, Nat. Commun. **6**, 8211 (2015).

[37] A. S. Shestakov, M. Schmid, D. Meier, T. Kuschel, and C. H. Back, Phys. Rev. B **92**, 224425 (2015).

[38] S. Y. Huang, W. G. Wang, S. F. Lee, J. Kwo, and C. L. Chien, Phys. Rev. Lett. **107**, 216604 (2011).

[39] A. D. Avery, M. R. Pufall, and B. L. Zink, Phys. Rev. Lett. **109**, 196602 (2012).

[40] A. Sola, M. Kuepferling, V. Basso, M. Pasquale, T. Kikkawa, K. Uchida, and E. Saitoh, J. Appl. Phys. **117**, 17C510 (2015).

[41] A. Sola, P. Bougiatioti, M. Kuepferling, D. Meier, G. Reiss, M. Pasquale, T. Kuschel, and V. Basso, Sci. Rep. **7**, 46752 (2017).

[42] B. Schulz and M. Hoffmann, High Temp. High Press. **34**, 203 (2002).

[43] A. T. Nelson, J. T. White, D. A. Andersson, J. A. Aguiar, K. J. McClellan, D. D. Byler, M. P. Short, and C. R. Stanek, J. Am. Ceram. Soc. **97**, 1559 (2014).

[44] O. Reimer, D. Meier, M. Bovender, L. Helmich, J.-O. Dreessen, J. Krieft, A. S. Shestakov, C. H. Back, J.-M. Schmalhorst, A. Hütten, G. Reiss, and T. Kuschel, Sci. Rep. **7**, 40586 (2017).

[45] T. Kuschel, C. Klewe, P. Bougiatioti, O. Kuschel, J. Wollschläger, L. Bouchenoire, S. D. Brown, J. M. Schmalhorst, D. Meier, and G. Reiss, IEEE Trans. Magn. **52**, 4500104 (2016).

[46] A. Prakash, B. Flebus, J. Brangham, F. Yang, Y. Tserkovnyak, and J. P. Heremans, arXiv:1706.09021.

[47] M. Meinert and G. Reiss, J. Phys. Condens. Matter **26**, 115503 (2014).

[48] H. Lord and R. Parker, Nature (London) **188**, 929 (1960).

[49] C. Klewe, T. Kuschel, J.-M. Schmalhorst, F. Bertram, O. Kuschel, J. Wollschläger, J. Strempfer, M. Meinert, and G. Reiss, Phys. Rev. B **93**, 214440 (2016).